Supplementary material
High-Coercivity Hexaferrite Ceramics Featuring Sub-Terahertz Ferromagnetic Resonance

Evgeny A. Gorbachev, Lev A. Trusov, Liudmila N. Alyabyeva,
Ilya V. Roslyakov, Vasilii A. Lebedev, Ekaterina S. Kozlyakova, Oxana V. Magdysyuk, Alexey V. Sobolev,
Iana S. Glazkova, Sergey A. Beloshapkin, Boris P. Gorshunov, and Pavel E. Kazin

Section 1. *Phase composition, microstructure, and mechanical properties vs sintering temperature*

The XRD reveals that the phase composition of the ceramics remains unchanged at sintering temperatures up to 1400 °C. At 1425 °C the magnetite phase Fe_3O_4 emerges, which content further increases with the temperature (**Fig. 1b**, **Fig. S6a**, **Table S2**). It was previously reported that unsubstituted strontium hexaferrite melts incongruently at 1435 °C in air and decomposes into a liquid and $SrFe_{18}O_{27}$ phase, which further transforms into Fe_3O_4 and liquid.[1] The similar process is also expected for $Sr_{0.67}Ca_{0.33}Fe_8Al_4O_{19}$. According to differential thermal analysis/thermogravimetry (DTA/TG), the pressed powder sample starts to melt at 1430 °C, which is accompanied by a loss of mass due to release of oxygen (**Fig. S9**). This leads to a partial reduction of Fe^{3+} to Fe^{2+} and the appearance of the magnetite phase, which is intensified at higher temperatures. At 1475 and 1500 °C the intensive hexaferrite melting and further solidification result in a separation of two hexaferrite phases with higher and lower aluminum content (HF1 and HF2, respectively). The compositions of these secondary hexaferrite phases can be estimated from the lattice parameters (**Fig. 1a**, **Fig. S10**) of reference samples [2,3] as $MFe_{7.7}Al_{4.3}O_{19}$ (HF1) and $MFe_{8.7}Al_{3.3}O_{19}$ (HF2) at 1475 °C and $MFe_{6.9}Al_{5.1}O_{19}$ (HF1) and $MFe_{8.7}Al_{3.3}O_{19}$ (HF2) at 1500 °C (M = Sr/Ca), which also correlates with the measured Curie temperatures (**Table S2**). Hence, single-phase $Sr_{0.67}Ca_{0.33}Fe_8Al_4O_{19}$ sintered ceramics form in the temperature range 1200 – 1400 °C.

The scanning electron microscopy (SEM) images of the powder and ceramics are presented in **Fig.1c-f** and **Fig. S11**. After heat treatment at temperatures below 1350 °C the particles are poorly sintered, and their mean diameters and particle size distributions are close to those observed in the initial powder (**Fig. S1**). At 1350 and 1400 °C the samples consist of tightly packed grains due to the formation of dense ceramics. At 1425 – 1500 °C, large tens-of-micrometers sized grains are formed within a matrix consisting of fine grains (**Fig. 1f**, **Fig. S12a**,**b**, **Fig. S11**, **Fig. S3**), which is the result of the so-called abnormal grain growth.[4] According to energy-dispersive x-ray spectroscopy (EDX) elemental analysis, the metal elements stoichiometry of the large grains corresponds well to a substituted hexaferrite phase with slightly higher concentration of Sr and Al compared to the matrix hexaferrite (**Fig. S13**). The electron backscattering diffraction (EBSD) analysis was used to probe the phase composition of the large grains and the surrounding fine-grained matrix (**Fig. S12**). It revealed that the large grains belong to M-type hexaferrite phase and showed that the grains are single crystals with different crystallographic orientations relative to the pellet surface, while the matrix consists of the hexaferrite phase too. Also, submicron particles incorporated into the large hexaferrite grains were found to be Fe_3O_4 phase, which is proved by EBSD (**Fig. S12e,c**) and EDX (**Fig. S12f-i**) analyses. The matrix hexaferrite grains have a plate-like morphology and their diameters (maximum dimensions) are increasing

with the sintering temperature (**Fig. S1**). While the fine matrix hexaferrite grains mostly remain below the single-domain limit at all sintering temperatures, the large grains significantly exceed it (**Fig. S3**).

According to the nanoindentation results, the pellets obtained are demonstrating consistent mechanical properties over the surface. For pellets annealed at 1300 °C and 1400 °C, Young modulus was found to be of 46 ± 8 GPa and 100 ± 20 GPa correspondingly (**Fig. S14**). The last is in a good agreement with previously reported values of 140 GPa for the dense non-substituted hexaferrite ceramics [1]. Hardness of 1.8 ± 0.7 и 4.3 ± 1.2 GPa has been measured. Higher uncertainty for the 1400 °C sample is caused by a presence of large particles. Therefore, we demonstrated that the proposed sintering method allows to obtain a ceramic pellets with appropriate mechanic properties.

Section 2. *Terahertz time-domain spectroscopy*

Parameters of magnetic resonance lines were obtained by processing the spectra of complex refraction index $n^*=n+ik$ of ceramic samples measured with commercial THz time-domain spectrometer Menlo Systems TERA K15. The resonance absorptions were modeled with a Lorentzian expression

$$\mu(f) = \mu'(f) + i\mu''(f) = \frac{\Delta\mu \cdot f_r^2}{f_r^2 - f^2 + i\Gamma f_r}, \qquad (1)$$

where f is the frequency, $\Delta\mu$ is the magnetic contribution, f_r is the resonance frequency and Γ is the damping factor.

Section 3. *Figures and tables.*

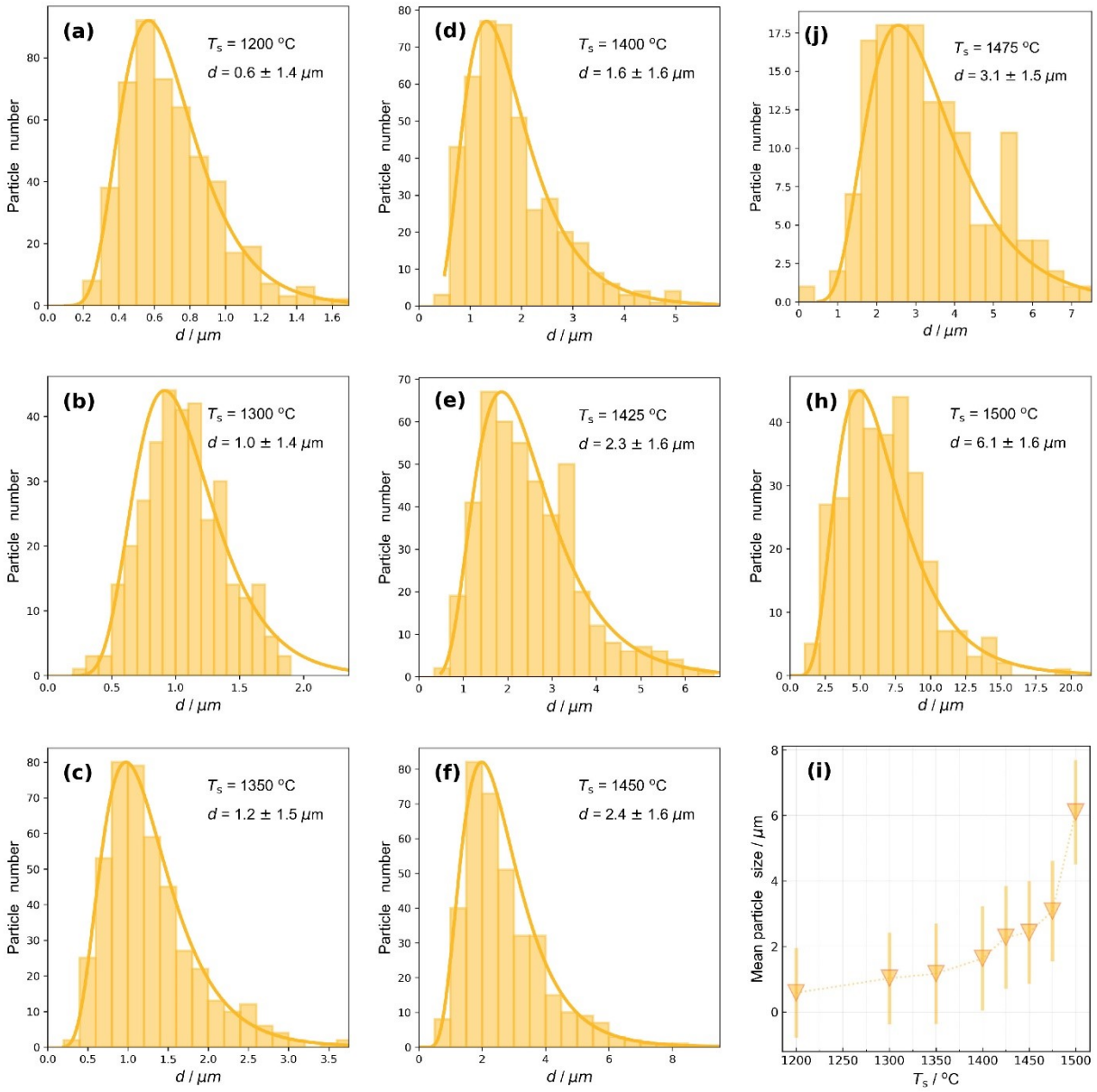

Figure S1. a-h) Matrix grain size distributions of ceramics. i) Mean matrix grain size vs sintering temperature (T_s).

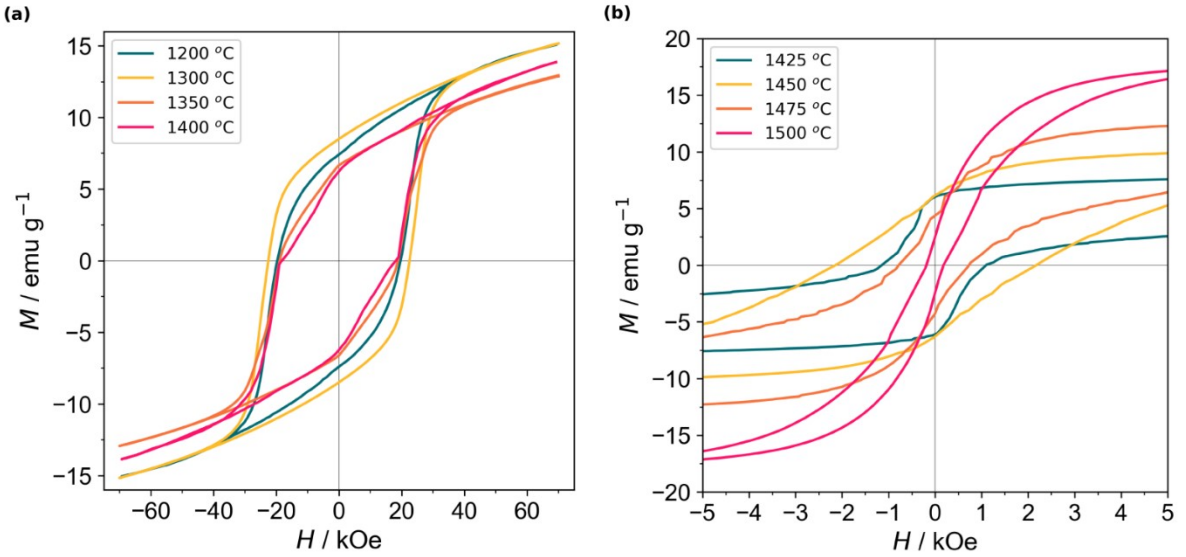

Figure S2. Magnetic hysteresis loops of hexaferrite ceramics obtained at 1200 – 1500 °C.

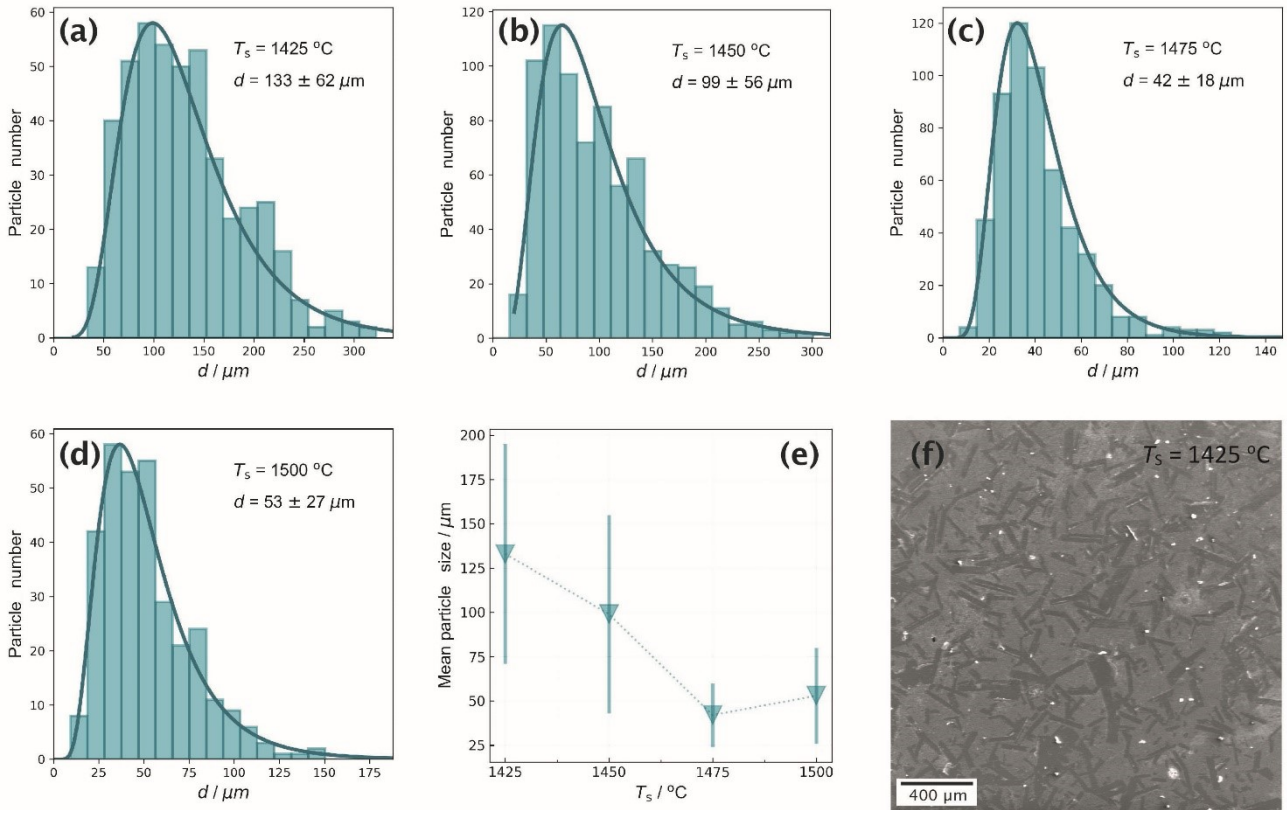

Figure S3. a-d) Size distribution of the secondary recrystallization grains within ceramic samples. e) Mean particle size *vs* sintering temperature (T_s). f) SEM image of the ceramic obtained at 1425 °C.

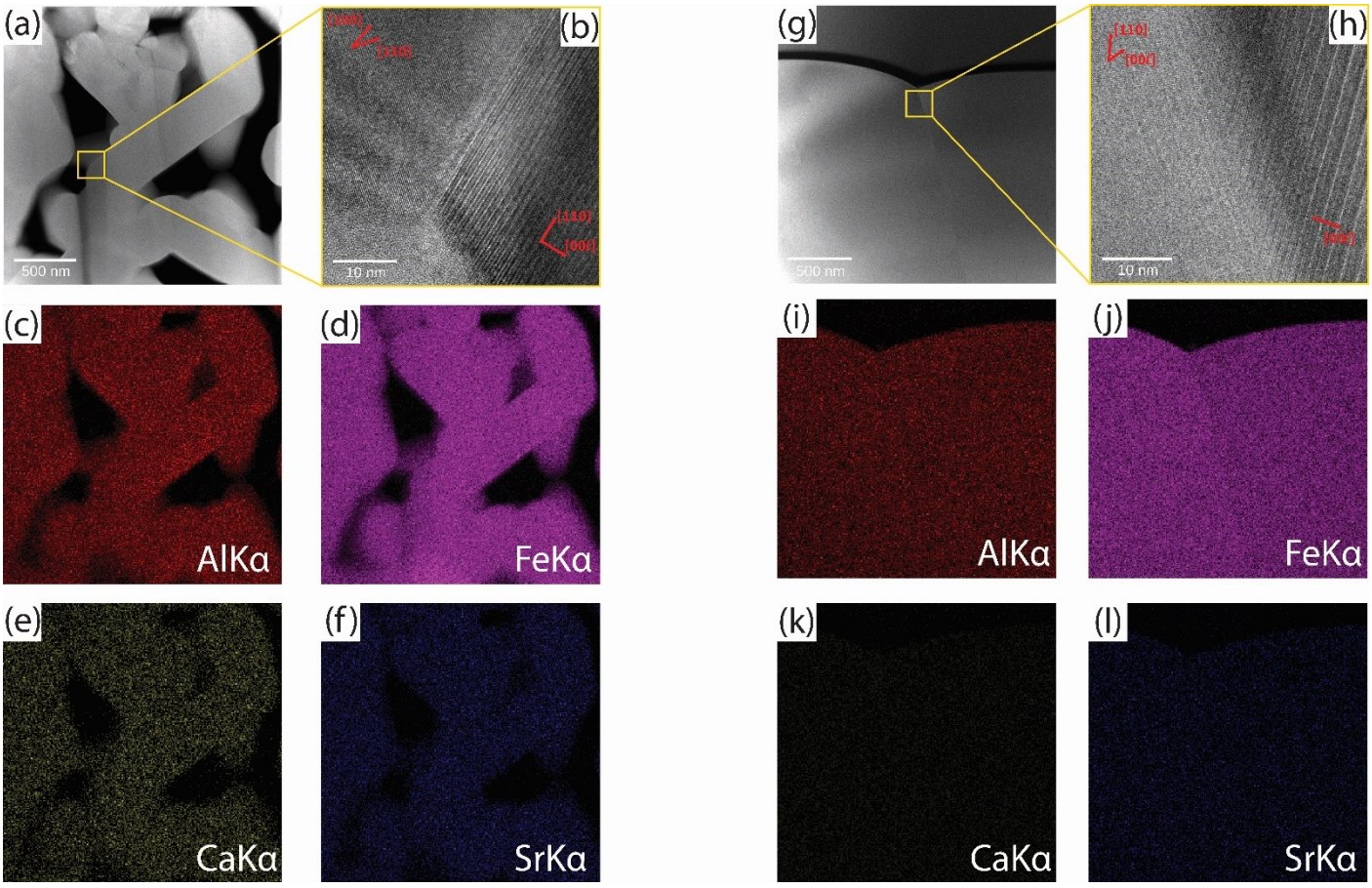

Figure S4. Scanning TEM (a, g), corresponding EDX maps (c – f, i – l) for Al, Fe, Ca, Sr elements, and corresponding high-resolution (b, h) TEM images of the hexaferrite grain interfaces within ceramics samples obtained at 1300 and 1400 °C, respectively.

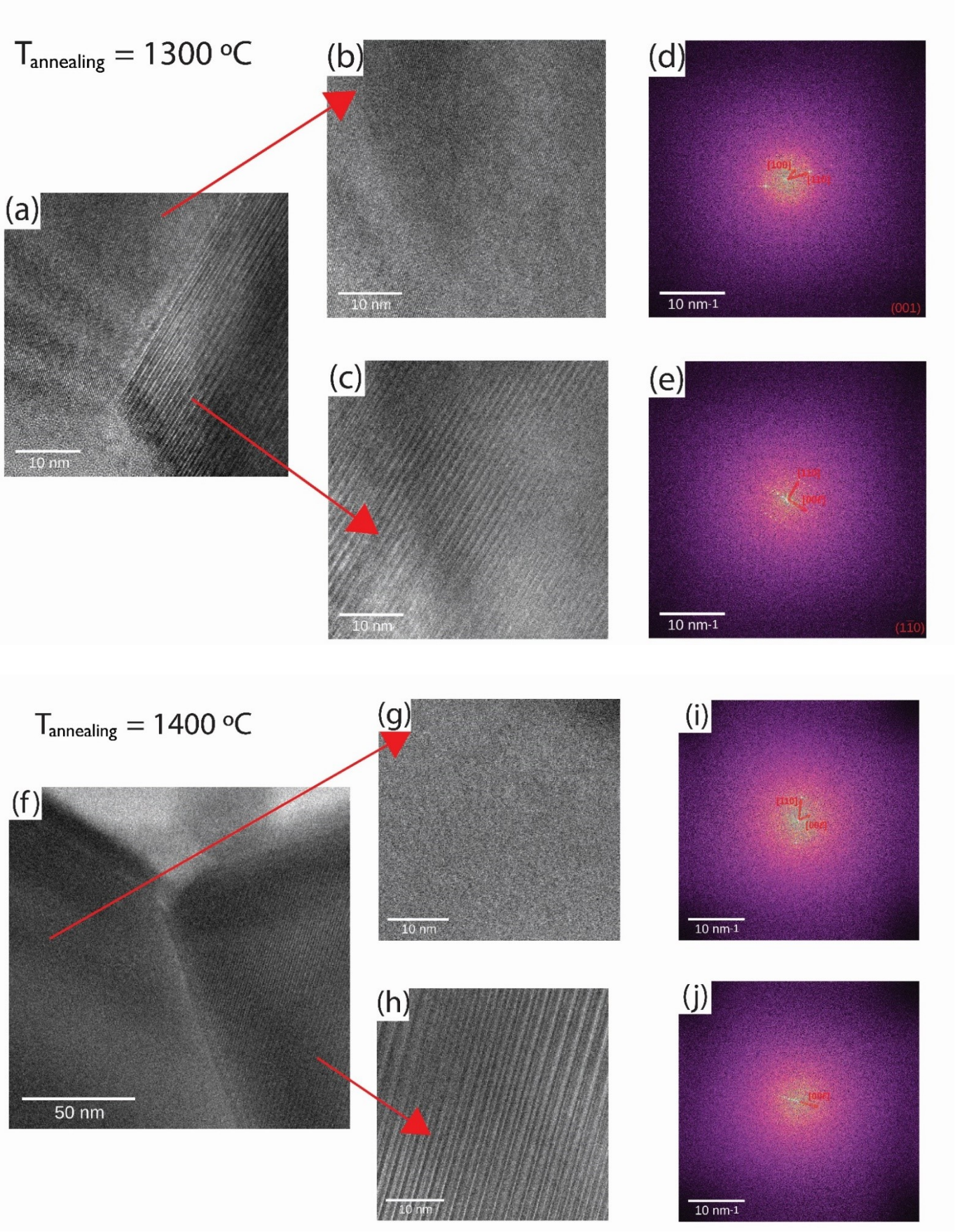

Figure S5. High-resolution TEM images (a-c and f-h) and FFT images (d, e and i, j) of ceramics samples obtained at 1300 and 1400 °C, respectively.

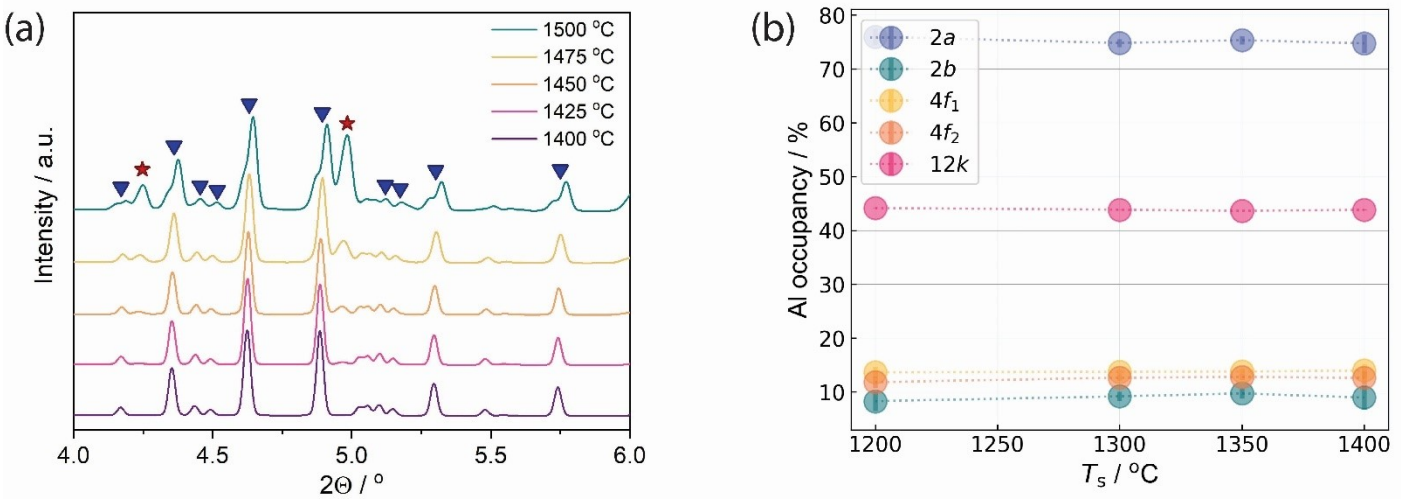

Figure S6. a) XRD phase analysis of ceramics obtained at different temperatures: triangles correspond to hexaferrite peaks, stars – peaks of magnetite phase; b) aluminum occupancies at iron sites within hexaferrites phase.

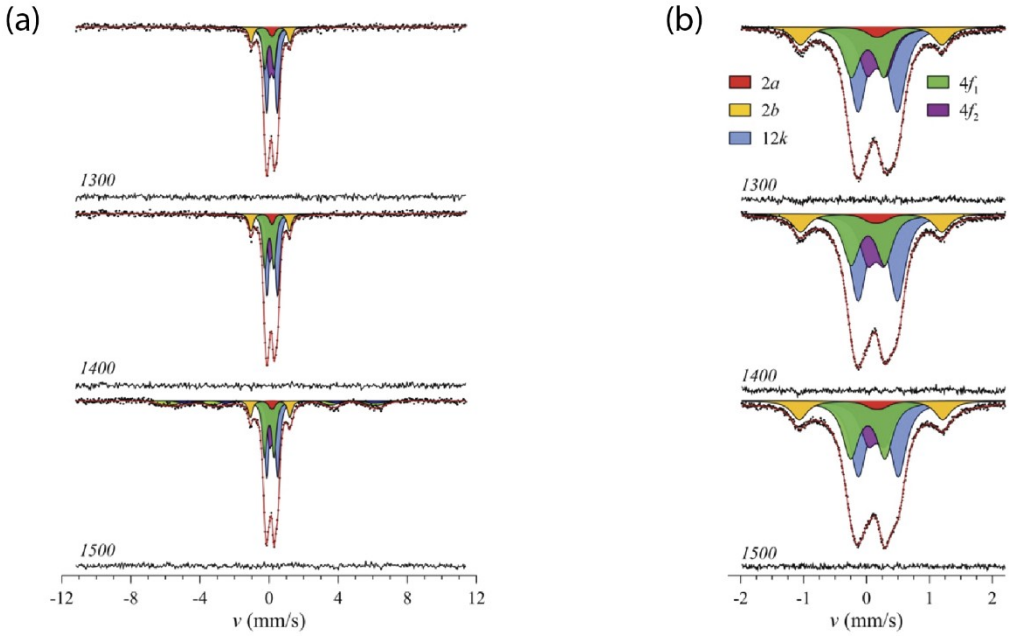

Figure S7. ^{57}Fe Mössbauer spectra of the hexaferrite ceramics obtained at 1300 °C, 1400 °C and 1500 °C, respectively, collected at 308 °C in a wide (a) and in a narrow (b) velocity range.

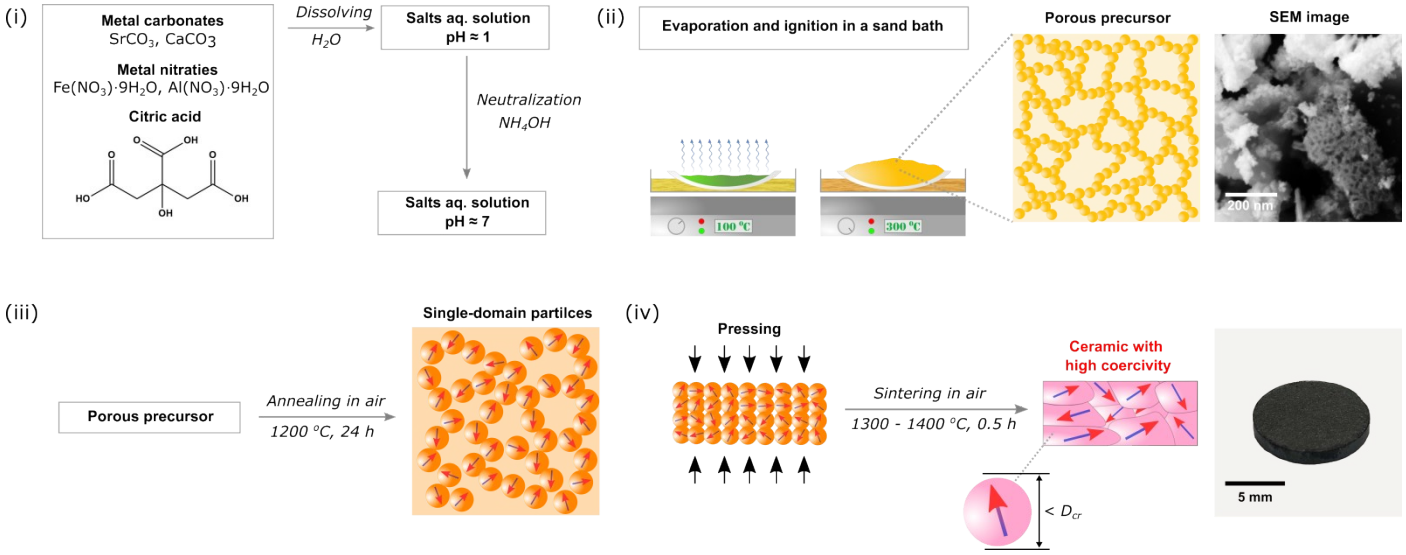

Figure S8. A flowchart showing the scheme to prepare an ultra-high coercivity dense ceramic of $Sr_{0.67}Ca_{0.33}Fe_8Al_4O_{19}$. (i) The citate solution is prepared and neutralized, (ii) the citate solution is evaporated to a citrate melt, then it is self-ignited to form an amorphous porous precursor. (iii) The porous precursor is annealed to get a powder of single-domain hexaferrite particles, (iv) the powder is pressed into a pellet, afterwards the pellet is sintered to produce a ceramic.

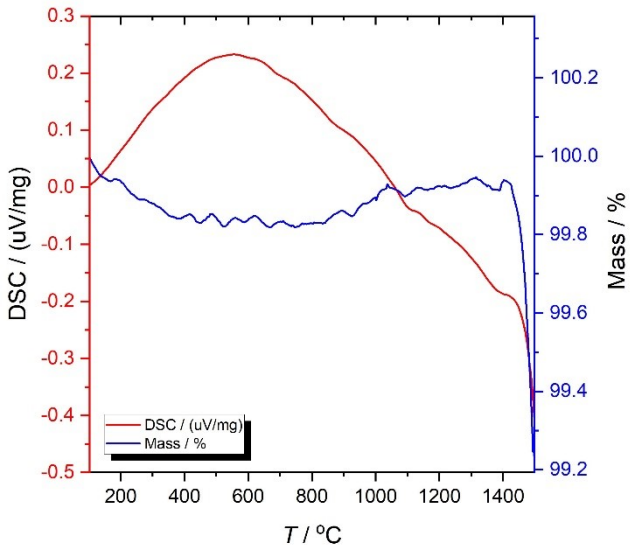

Figure S9. DTA analysis of pressed powder of hexaferrite.

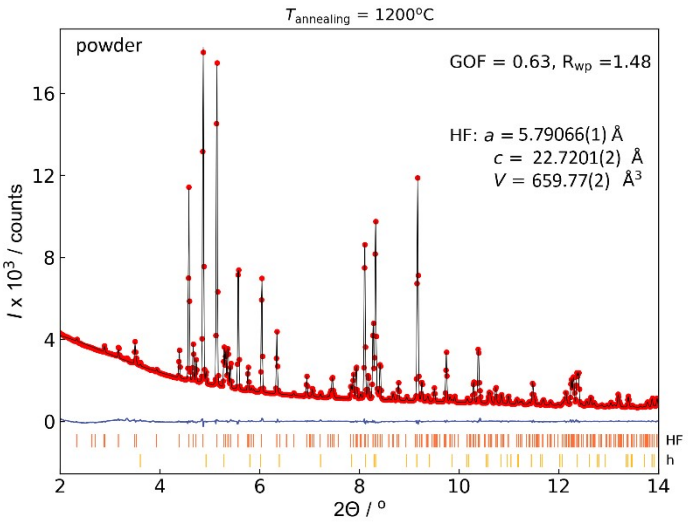
$T_{annealing}$ = 1200°C
powder
GOF = 0.63, R_{wp} =1.48
HF: a = 5.79066(1) Å
c = 22.7201(2) Å
V = 659.77(2) Å^3
I x 10^3 / counts
2Θ / °
HF
h

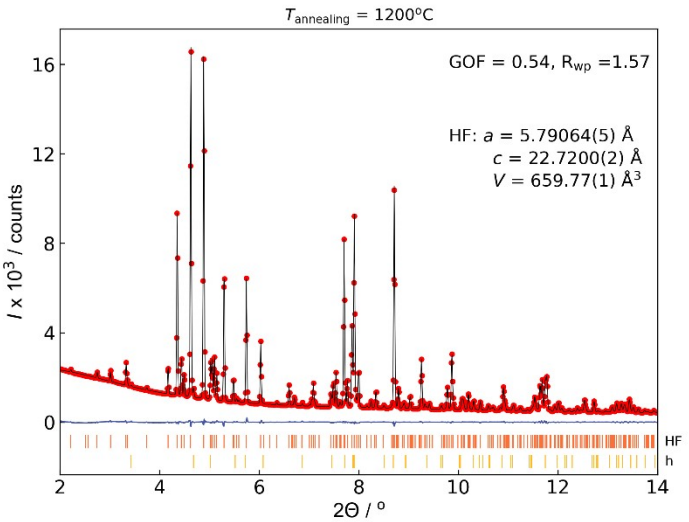
$T_{annealing}$ = 1200°C
GOF = 0.54, R_{wp} =1.57
HF: a = 5.79064(5) Å
c = 22.7200(2) Å
V = 659.77(1) Å^3
I x 10^3 / counts
2Θ / °
HF
h

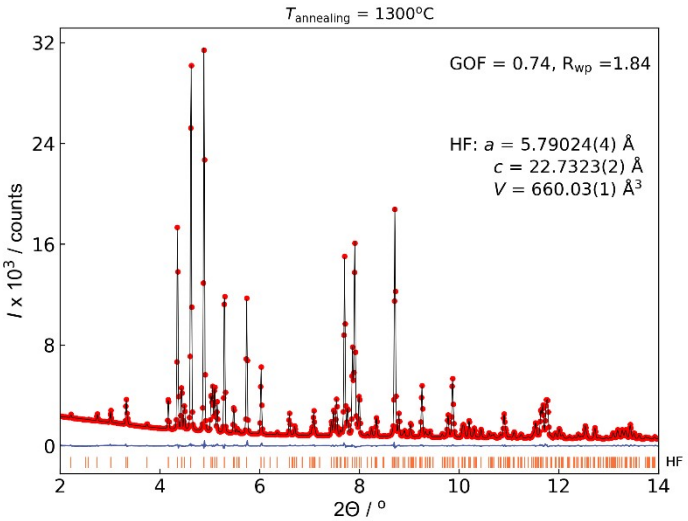
$T_{annealing}$ = 1300°C
GOF = 0.74, R_{wp} =1.84
HF: a = 5.79024(4) Å
c = 22.7323(2) Å
V = 660.03(1) Å^3
I x 10^3 / counts
2Θ / °
HF

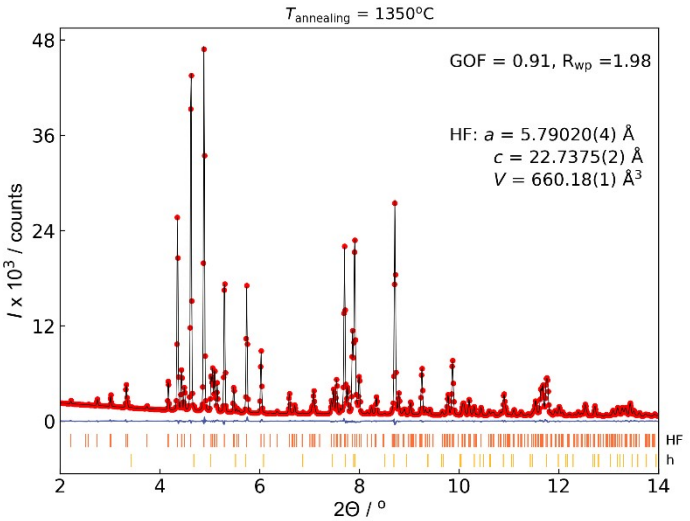
$T_{annealing}$ = 1350°C
GOF = 0.91, R_{wp} =1.98
HF: a = 5.79020(4) Å
c = 22.7375(2) Å
V = 660.18(1) Å^3
I x 10^3 / counts
2Θ / °
HF
h

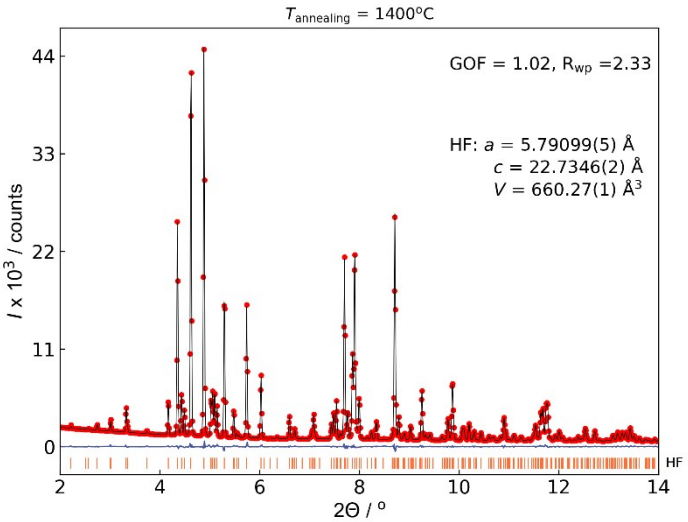
$T_{annealing}$ = 1400°C
GOF = 1.02, R_{wp} =2.33
HF: a = 5.79099(5) Å
c = 22.7346(2) Å
V = 660.27(1) Å^3
I x 10^3 / counts
2Θ / °
HF

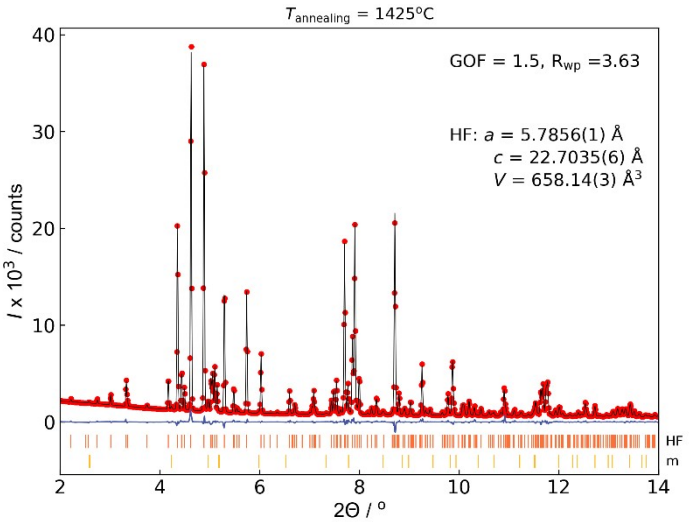
$T_{annealing}$ = 1425°C
GOF = 1.5, R_{wp} =3.63
HF: a = 5.7856(1) Å
c = 22.7035(6) Å
V = 658.14(3) Å^3
I x 10^3 / counts
2Θ / °
HF
m

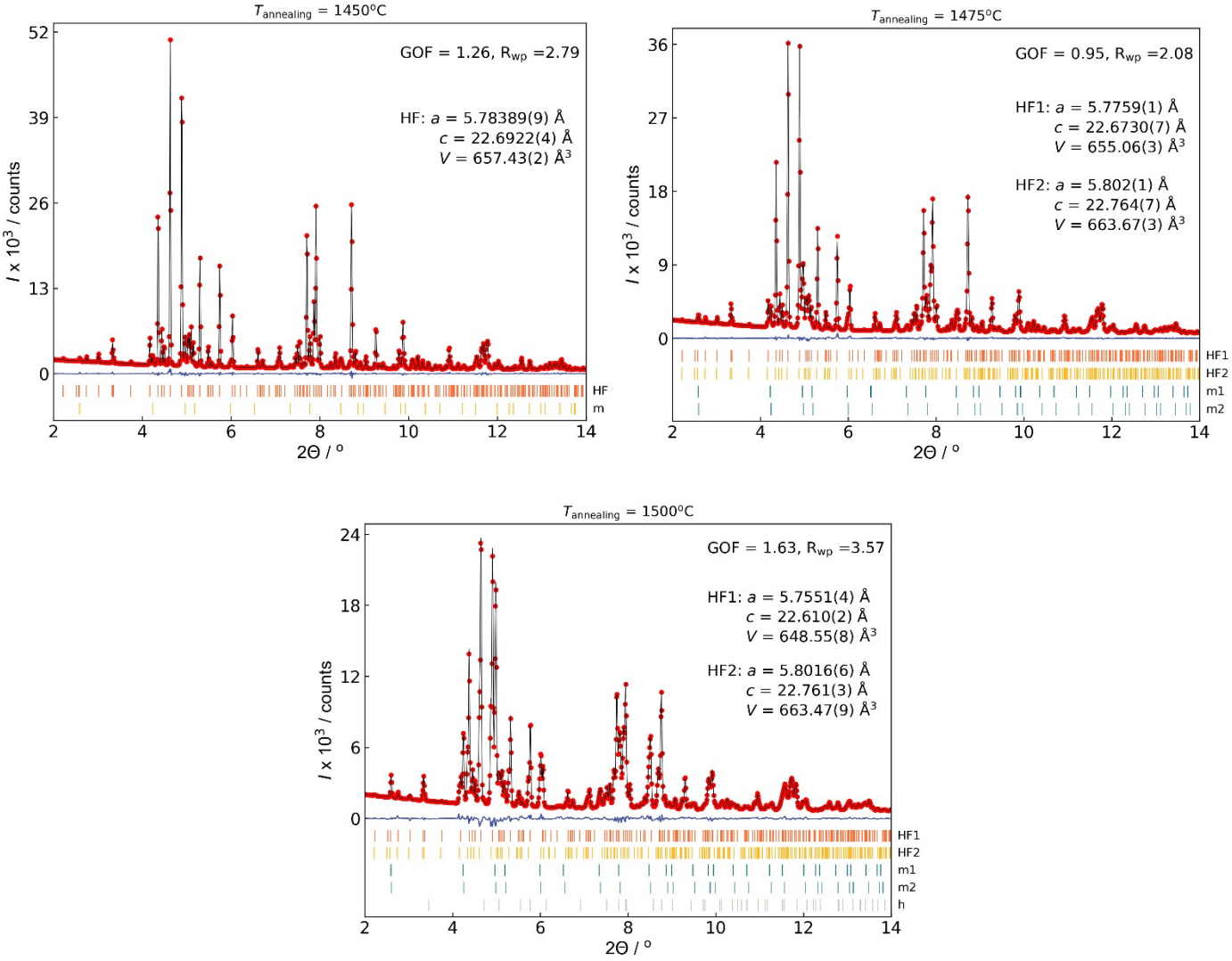

Figure S10. XRD patterns and Rietveld analyses of powder and ceramic samples with nominal composition of $Sr_{1-x/12}Ca_{x/12}Fe_{12-x}Al_xO_{19}$ ($x = 4$). Red circles, black lines, and blue lines are the observed patterns, calculated patterns, and their differences, respectively. Bars labeled as "HF", "h", "m" represent the calculated positions of the Bragg reflections for main hexaferrite phase and secondary phases of α-Fe_2O_3, Fe_3O_4, respectively.

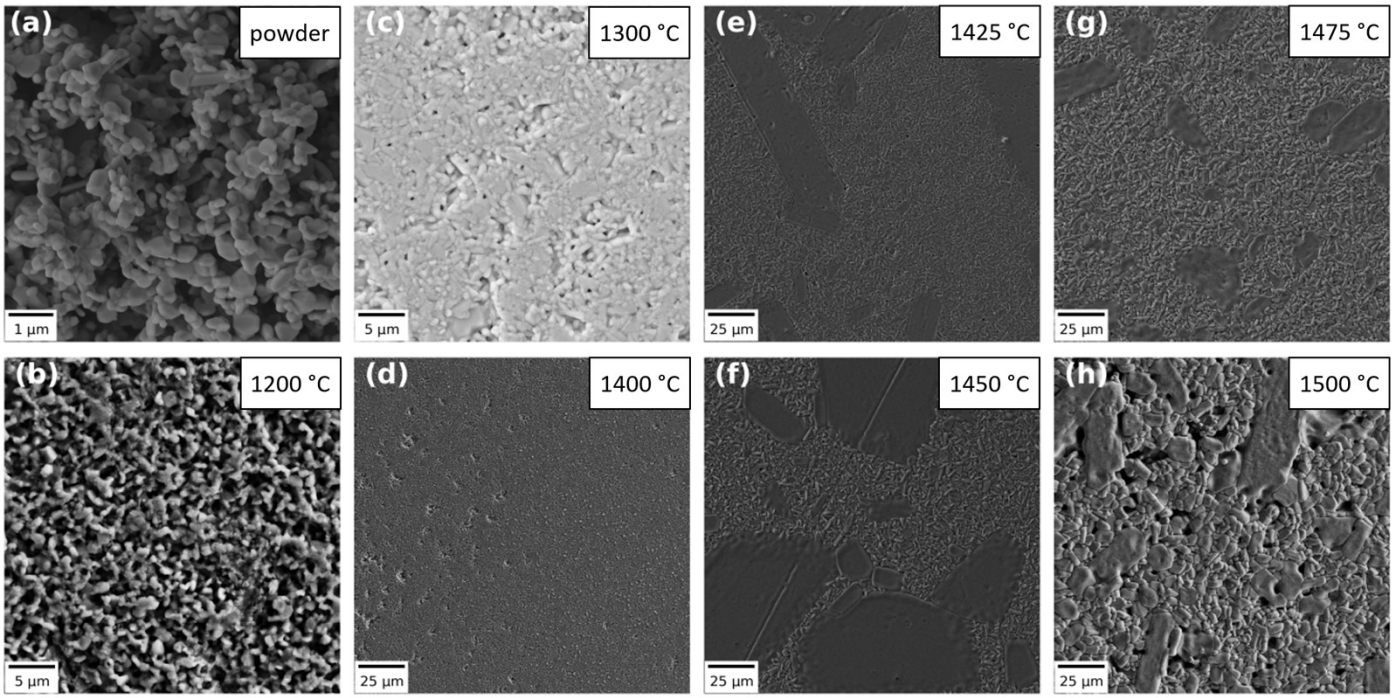

Figure S11. SEM images of powder (a) and ceramics samples (b – c) obtained at 1200 – 1500 °C, respectively.

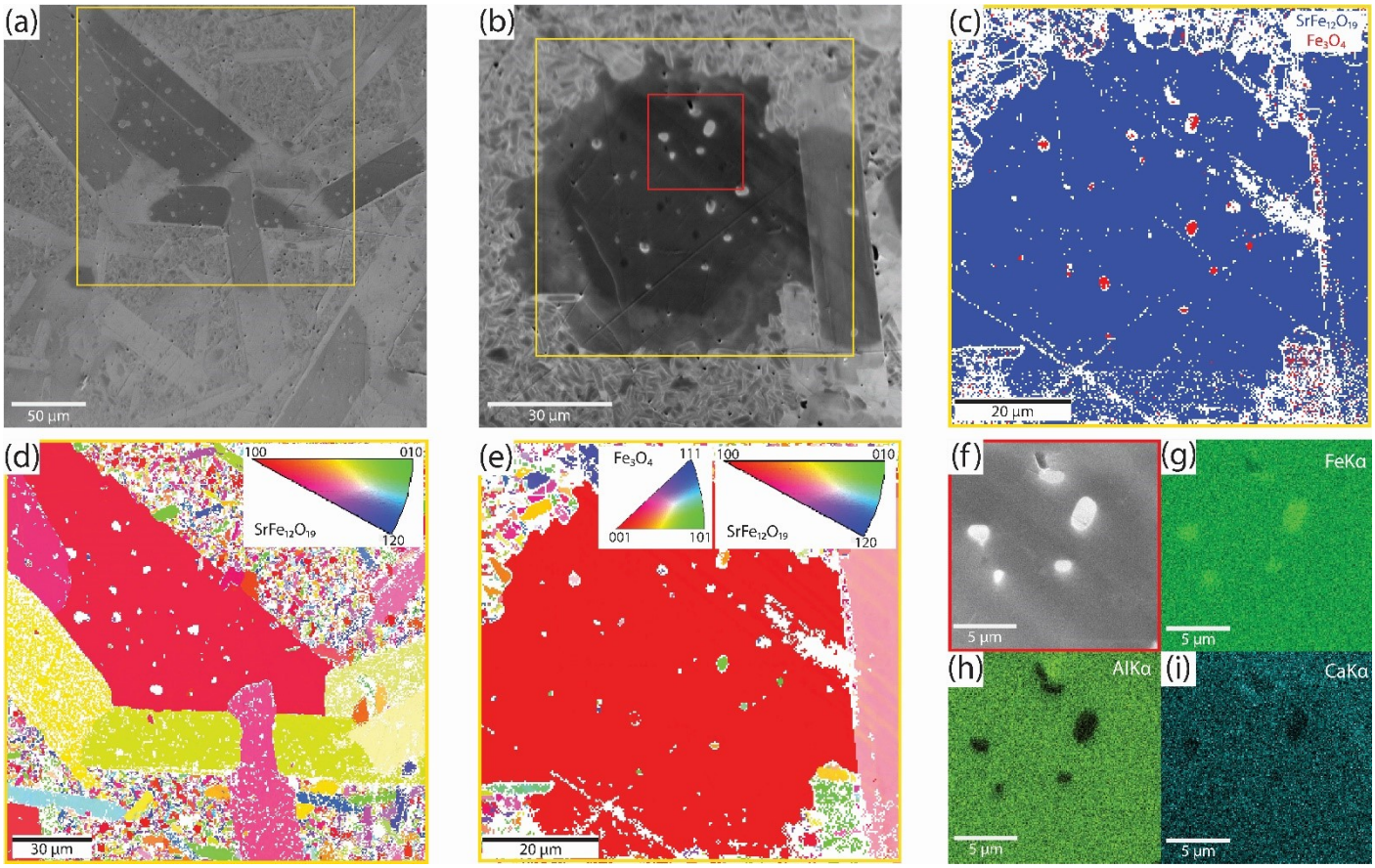

Figure S12. SEM images (a, b) and corresponded EBSD maps (d, e) with 0.5 μm (d) and 0.3 μm (c, e) steps for $SrFe_{12}O_{19}$ and Fe_3O_4 phases (ISCD 66403 and ISCD 50567, respectively). The colors refer to the orientations shown by the inverse pole figures (inserts); (c) EBSD phase color map for $SrFe_{12}O_{19}$ (blue) and Fe_3O_4 (red); f) SEM image from the red area on picture (b) and corresponding EDX maps (g – i) for Al, Fe, Ca elements.

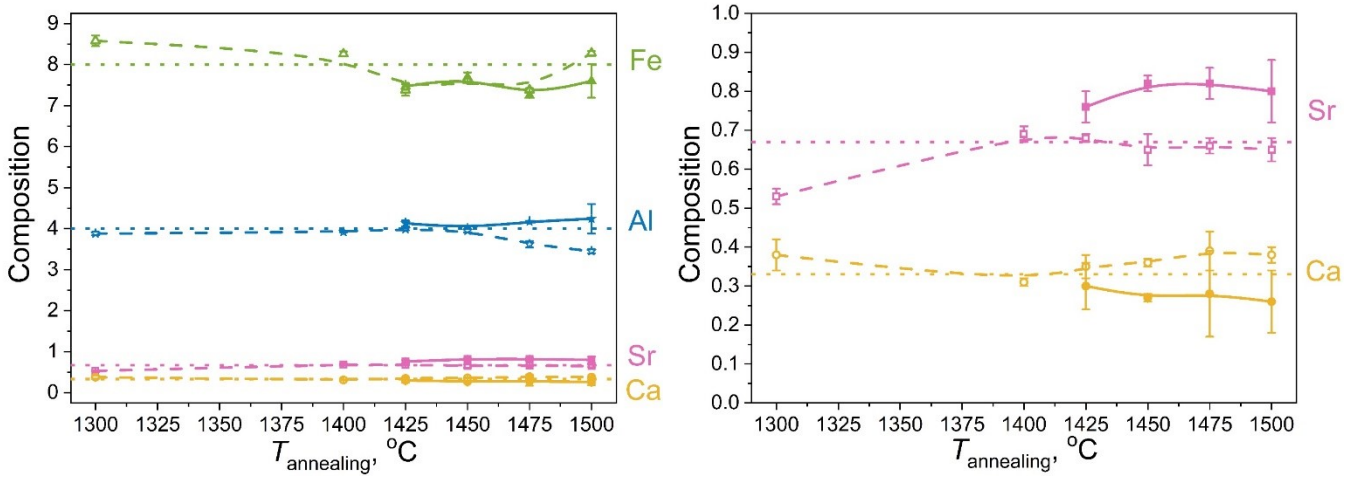

Figure S13. Content of atoms per hexaferrite formula unit ($SrFe_{12}O_{19}$) calculated from the EDX analysis of the ceramic samples obtained at different temperatures. Dotted lines correspond to atom content within matrix, while solid lines are attributed to that within large tens-of-microns hexaferrite grains.

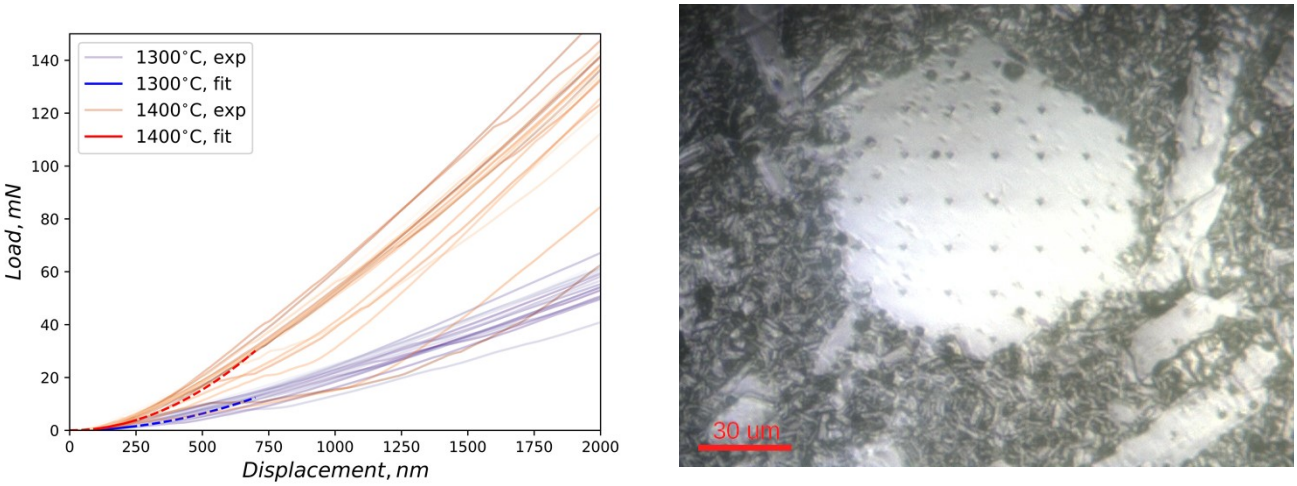

Figure S14. Load-displacement curves, acquired by the nanoindentation method from different points over the surface of ceramic pellets obtained at 1300 and 1400 °C, and an example of the post-indentation micrograph.

Table S1. Properties of the ceramics: d – average grain diameter, ρ – specific density, w – relative phase amount in mass %.

T_s (°C)	d (μm)	ρ* (%)	w(HF1), %	w(HF2), %	w(α-Fe_2O_3), %	w(Fe_3O_4), %
1200	0.6(1.4)	55	98.9(1)	-	1.1(3)	-
1300	1.7(1.4)	67	100	-	-	-
1350	2.1(1.5)	77	99.8(2)	-	0.2(2)	-
1400	3.1(1.5)	95	100	-	-	-
1425	2.3(1.6)	95	98.7(1)	-	-	1.3(3)
1450	2.4(1.6)	95	95.8(2)	-	-	4.2(2)
1475	3.1(1.6)	95	78.7(2)	9.5(3)	-	11.8(3)
1500	6.1(1.5)	95	55.6(2)	21.3(3)	0.1(2)	23.0(3)

*specific densities were calculated as $m \cdot V^{-1} \cdot \rho^{-1} \cdot 100\%$, where m – mass of a ceramic sample, V – volume of a ceramic sample, ρ – crystallographic density of a ceramic sample. HF1 and HF2 – hexaferrite phases.

Table S2. The Curie temperatures of hexaferrite (HF1, HF2) and magnetite (m1, m2) phases within the ceramic samples sintered at various temperatures (T_s).

T_s, ºC	T_C (HF1), ºC	T_C (HF2), ºC	T_C (m1), ºC	T_C (m2), ºC
1200	223	-	-	-
1300	227	-	-	-
1350	235	-	-	-
1400	236	-	-	-
1425	232	-	519	-
1450	229	-	527	-
1475	214	285	524	508
1500	165	290	562	478

HF1 – the main hexaferrite phase, HF2 – the secondary hexaferrite phase, m1 – the magnetite phase with lower aluminum content, m2 – the magnetite phase with higher aluminum content.

Table S3. Parameters of $Sr_{0.67}Ca_{0.33}Fe_8Al_4O_{19}$ ceramic samples: magnetic properties (H_C – the coercivity, M_S – the saturation magnetization, M_r – the remanence) and fitting lines of the natural ferromagnetic resonance with Lorentzian expression for complex magnetic permeability $\mu^*(f) = \Delta\mu f_r^2(f_r^2-f^2+ifT)^{-1}$, ($f_r$ – the resonance frequency, $\Delta\mu$ – the magnetic strength or magnetic contribution of the resonance, Γ – the damping factor with errors in brackets).

T_s (ºC)	H_C (kOe)	M_S (emu g^{-1})	M_R (emu g^{-1})	M_{SV} (emu cm^{-3})	$(BH)_{max}$ (kGOe)	M_r/M_S	f_r (GHz)	Γ (GHz)	$\Delta\mu$ x 10^{-3}	$Q = f_r/\gamma$
1200	19.6	15.0	7.6	39	19.2	0.51	160(3)	15(1)	4.8(5)	11
1300	22.5	15.0	8.5	47	28.1	0.57	163(3)	9(2)	7(1)	18
1350	18.9	13.9	6.7	50	23.0	0.48	198(3)	9(2)	7(1)	18
1400	18.2	12.9	6.2	58	29.6	0.48	200(3)	8(2)	7(1)	25
1425	1.1	11.6	6	–	–	0.52	205(3)	6(2)	7(1)	34
1450	2.1	14.2	6.2	–	–	0.44	214(3)	12(3)	7(1)	18
1475	0.8	15.9	4.4	–	–	0.28	224(3) 282(3)	25(3)	7(1)	9 11
1500	0.2	20.8	1.0	–	–	0.05	–	–	–	–

Table S4. The ^{57}Fe hyperfine parameters of the hexaferrite $Sr_{0.67}Ca_{0.33}Fe_8Al_4O_{19}$ samples obtained at different temperatures.

T (°C)	Site	d (mm/s)	D (mm/s)	D_{theor} (mm/s)	B_{hf} (kOe)	I (%)	occup.
1300	2*a*	0.17(3)	0.13(10)	0.01	-	3.10(4)	0.248(4)
	2*b*	0.075(3)	2.25(1)	2.22	-	9.3(3)	0.75(2)
	$4f_1$	0.019(9)	0.52(2)	0.37	-	24(2)	0.98(9)
	$4f_2$	0.16(1)	0.31(1)	0.28	-	21.5(3)	0.86(1)
	12*k*	0.179(5)	0.627(3)	0.62	-	42(2)	0.83(4)
1400	2*a*	0.15(3)	0.18(8)	0.01	-	3.11(4)	0.248(3)
	2*b*	0.075(3)	2.25(1)	2.22	-	9.2(3)	0.73(2)
	$4f_1$	0.023(3)	0.53(1)	0.37	-	24(1)	0.98(4)
	$4f_2$	0.154(3)	0.27(1)	0.28	-	21.6(2)	0.86(1)
	12*k*	0.180(2)	0.627(2)	0.62	-	41.8(8)	0.84(2)
1500	2*a*	0.17(3)	0.15(7)	0.01	-	2.35(5)	0.228(3)
	2*b*	0.073(3)	2.28(1)	2.22	-	7.1(3)	0.80(2)
	$4f_1$	0.021(3)	0.55(1)	0.37	-	23.2(7)	1.1(1)
	$4f_2$	0.161(3)	0.26(1)	0.28	-	16.3(3)	0.79(1)
	12*k*	0.189(2)	0.636(2)	0.62	-	31.7(6)	0.77(1)
	"+3" sp.	0.16(6)	0.0(2)*	-	367(12)	12.9(3)	-
	"+2.5" sp.	0.7(1)	0.0(1)*	-	323(18)	6(1)	-

Table S5. Properties of commonly used hard-magnetic materials at 300 K: the saturation magnetization M_S, the remanence M_r, the coercivity H_C, the maximum energy product $(BH)_{max}$, the Curie temperature T_C and the natural ferromagnetic resonance frequency f_r.

Material	M_S, **emu/g**	H_C, **kOe**	$(BH)_{max}$, **MGOe**	T_C, **K**	f_r, **GHz**	**References**
Nd-Fe-B	168	8 - 20	50	585	-	[5], [6]
Sm-Co	107	5-7	15 - 25	1000	-	[5]
Fe-Pt	60	9	51	750	-	[7], [6]
Mn-Bi	75	11	7.1	-	-	[8]
ε-Fe_2O_3	15	20	-	490	180	[5]
$SrFe_{12}O_{19}$	74	5	1	740	51	[9], [10]
$Sr_{0.67}Ca_{0.33}Fe_8Al_4O_{19}$*	13.9	18.9	0.023	508	200	this work

*the sample obtained in this work at the annealing temperature of 1350 °C.

References

[1] K. Kojima, Handbook of Magnetic Materials Volume 3, North-Holland Publishing Company, 1982.
[2] F. Sandiumenge, S. Gali, J. Rodriguez, Mater. Res. Bull. 23 (1988) 685–692.
[3] E.A. Gorbachev, L.A. Trusov, A.E. Sleptsova, E.S. Kozlyakova, L.N. Alyabyeva, S.R. Yegiyan, A.S. Prokhorov, V.A. Lebedev, I. V. Roslyakov, A. V. Vasiliev, P.E. Kazin, Mater. Today 32 (2020) 13–18.
[4] W.D. Kingery, H.K. Bowen, D.R. Uhlmann, Intoduction to Ceramics, Wiley, New York, 1976.
[5] E.A. Gorbachev, E.S. Kozlyakova, L.A. Trusov, A.E. Sleptsova, M.A. Zykin, P.E. Kazin, Russ. Chem. Rev. 90 (2021) 1287–1329.
[6] T. Klemmer, D. Hoydick, H. Okumura, B. Zhang, W.A. Soffa, Scr. Metall. Mater. 33 (1995) 1793–1805.
[7] N. Hoang Nam, N. Thi Thanh Van, N. Dang Phu, T. Thi Hong, N. Hoang Hai, N.H. Luong, J. Nanomater. 2012 (2012) 1–4.
[8] Y.B. Yang, X.G. Chen, R. Wu, J.Z. Wei, X.B. Ma, J.Z. Han, H.L. Du, S.Q. Liu, C.S. Wang, Y.C. Yang, Y. Zhang, J.B. Yang, J. Appl. Phys. 111 (2012) 07E312.
[9] B. Abraime, M. Ait Tamerd, A. Mahmoud, F. Boschini, A. Benyoussef, M. Hamedoun, Y. Xiao, A. El Kenz, O. Mounkachi, Ceram. Int. 43 (2017) 15999–16006.
[10] E.A. Gorbachev, L.A. Trusov, M. Wu, A. V. Vasiliev, R.D. Svetogorov, L.N. Alyabyeva, V.A. Lebedev, A.E. Sleptsova, M.A. Karpov, Y.M. Mozharov, B.P. Gorshunov, P.E. Kazin, J. Mater. Chem. C 9 (2021) 13832–13840.